



HAL
open science

T-matrix and Hapke Modeling of the Thermal Infrared Spectra of Trojan Asteroids and (944) Hidalgo: Implications for Their Regolith Particle Size and Porosity

Vanessa C. Lowry, Kerri L. Donaldson Hanna, Gen Ito, Michael S. P. Kelley, Humberto Campins, Sean Lindsay

► To cite this version:

Vanessa C. Lowry, Kerri L. Donaldson Hanna, Gen Ito, Michael S. P. Kelley, Humberto Campins, et al.. T-matrix and Hapke Modeling of the Thermal Infrared Spectra of Trojan Asteroids and (944) Hidalgo: Implications for Their Regolith Particle Size and Porosity. *The Planetary Science Journal*, 2022, 3, pp.1-14. 10.3847/PSJ/ac7a30 . insu-03777751

HAL Id: insu-03777751

<https://insu.hal.science/insu-03777751>

Submitted on 15 Sep 2022

HAL is a multi-disciplinary open access archive for the deposit and dissemination of scientific research documents, whether they are published or not. The documents may come from teaching and research institutions in France or abroad, or from public or private research centers.

L'archive ouverte pluridisciplinaire **HAL**, est destinée au dépôt et à la diffusion de documents scientifiques de niveau recherche, publiés ou non, émanant des établissements d'enseignement et de recherche français ou étrangers, des laboratoires publics ou privés.



Distributed under a Creative Commons Attribution 4.0 International License



T-matrix and Hapke Modeling of the Thermal Infrared Spectra of Trojan Asteroids and (944) Hidalgo: Implications for Their Regolith Particle Size and Porosity

Vanessa C. Lowry¹ , Kerri L. Donaldson Hanna¹, Gen Ito² , Michael S. P. Kelley³ , Humberto Campins¹, and Sean Lindsay⁴

¹University of Central Florida, Orlando, FL 32816, USA; vanessa_lowry@knights.ucf.edu

²Centre de Recherche Pétrographiques et Géochimiques (CRPG), Centre National de la Recherche Scientifique (CNRS)/Université de Lorraine, Vandoeuvre-lès-Nancy F-54501, France

³University of Maryland, College Park, MD 20783, USA

⁴University of Tennessee, Knoxville, TN 37996, USA

Received 2022 April 8; revised 2022 June 2; accepted 2022 June 16; published 2022 July 29

Abstract

Trojan asteroids (911) Agamemnon, (1172) Aeneas, and (624) Hektor and primitive asteroid (944) Hidalgo share a common thermal infrared spectral feature: a prominent 10 μm plateau that is also present in cometary comae spectra. To fit these asteroid spectra, we modeled individual minerals using the light-scattering multiple sphere T-matrix (MSTM) and Hapke reflectance models. Modeled mineral spectra were then combined using a weighted least-squares (WLS) model that included a spectral library of varied particle sizes and porosities. We later refined our method by using the mineral abundances, particle sizes, and porosities computed by WLS as an input to rerun the MSTM and Hapke models. We were able to model the asteroid spectral features using a mixture of olivine components, fine particles, and lunar-like porosities. The Trojan asteroids and (944) Hidalgo are comparable in mineral composition and particle size to spectrally similar bodies such as comet Hale-Bopp and CO3 and CY chondrite meteorites. While the required porosities for modeling are like those present on the lunar surface, they are lower than those in the meteorites and higher than those in comets.

Unified Astronomy Thesaurus concepts: [Jupiter trojans \(874\)](#); [Astronomy data modeling \(1859\)](#); [Spectroscopy \(1558\)](#)

1. Introduction

The Jupiter Trojan asteroids and primitive asteroid (944) Hidalgo represent some of the most pristine objects in our solar system (e.g., Emery et al. 2006; Rivkin et al. 2009). The Trojan asteroids exist in a region where there is a transition of rocky to icy material, making them an interesting target of study (e.g., Emery et al. 2006; Rivkin et al. 2009). Although there exist many hypotheses regarding the origin of the Trojan asteroids (Marzari et al. 2002; Emery et al. 2006, and references therein), the most widely accepted theory of their origin is that they are planetesimals trapped during the formation of Jupiter (Marzari et al. 2002). While (944) Hidalgo is not a Jupiter Trojan asteroid, it is relevant to this study, since it is spectrally similar to the Trojans and thought to be the remnant of an extinct comet (Campins et al. 2005; Hargrove et al. 2008). Thus, determining the composition of the Trojan asteroids is important for understanding the conditions of the solar nebula in the Jupiter region and their connection with spectrally similar bodies like (944) Hidalgo (Emery et al. 2006; Campins et al. 2007).

Previous reflectance studies of the Trojan asteroids and (944) Hidalgo in the visible to near-infrared regions of the electromagnetic spectrum showed no distinctive absorption features indicative of composition, although their observed red spectral slopes (increasing reflectance as wavelength increases) could indicate the presence of silicates (Emery & Brown 2004; Campins et al. 2005; Emery et al. 2006, and references therein). The Trojans show two different spectral types that vary in their

spectral slopes: a “red” type and a less red type, referred to as the “gray” type (Emery et al. 2011). The Trojan asteroids modeled in this study are of the red type (Emery et al. 2011).

The spectral features present over the thermal infrared (TIR) portion of the electromagnetic spectrum are useful in determining silicate mineralogies (e.g., Lyon 1964; Conel 1969; Salisbury & Walter 1989; Moersch & Christensen 1995; Wald & Salisbury 1995; Mustard & Hays 1997; Hamilton 2000), and their contrast, shape, and position are affected by mineral chemistry, albedo, particle size, porosity, and the near-surface thermal environment (e.g., Salisbury & Eastes 1985; Carrier et al. 1991; Salisbury & Wald 1992; Sprague et al. 1992; Hapke 1993; Henderson & Jakosky 1994). Spectral features in the TIR have been used to identify silicate minerals via remote sensing for the Moon, asteroids, comets, and Mars (e.g., Crovisier et al. 1997; Christensen et al. 2001, 2005; Sprague et al. 2002; Watanabe & Matsuo 2003). The Jupiter Trojan asteroids share a prominent 10 μm plateau with each other that is qualitatively similar to the spectra of (944) Hidalgo, cometary comae, and other primitive main belt asteroids (Emery et al. 2006; Campins et al. 2007; Licandro et al. 2012). An example of a primitive main belt asteroid family that is spectrally similar to the Trojan asteroids is the Themis family (Licandro et al. 2012). The Themis family shows a plateau near 10 μm when observed over the 5–14 μm region using the Spitzer Space Telescope (Licandro et al. 2012), but the feature is not as prominent as the asteroids in this study (e.g., Emery et al. 2006). In addition to other asteroids, the Trojan asteroids and (944) Hidalgo also share the 10 μm plateau with outer solar system bodies like short-period comets, Centaurs, and trans-Neptunian objects with low albedos (Marzari et al. 2002).

The Trojan asteroids not only share similar spectral features with each other, but they are all in stable orbits around Jupiter



Original content from this work may be used under the terms of the [Creative Commons Attribution 4.0 licence](#). Any further distribution of this work must maintain attribution to the author(s) and the title of the work, journal citation and DOI.

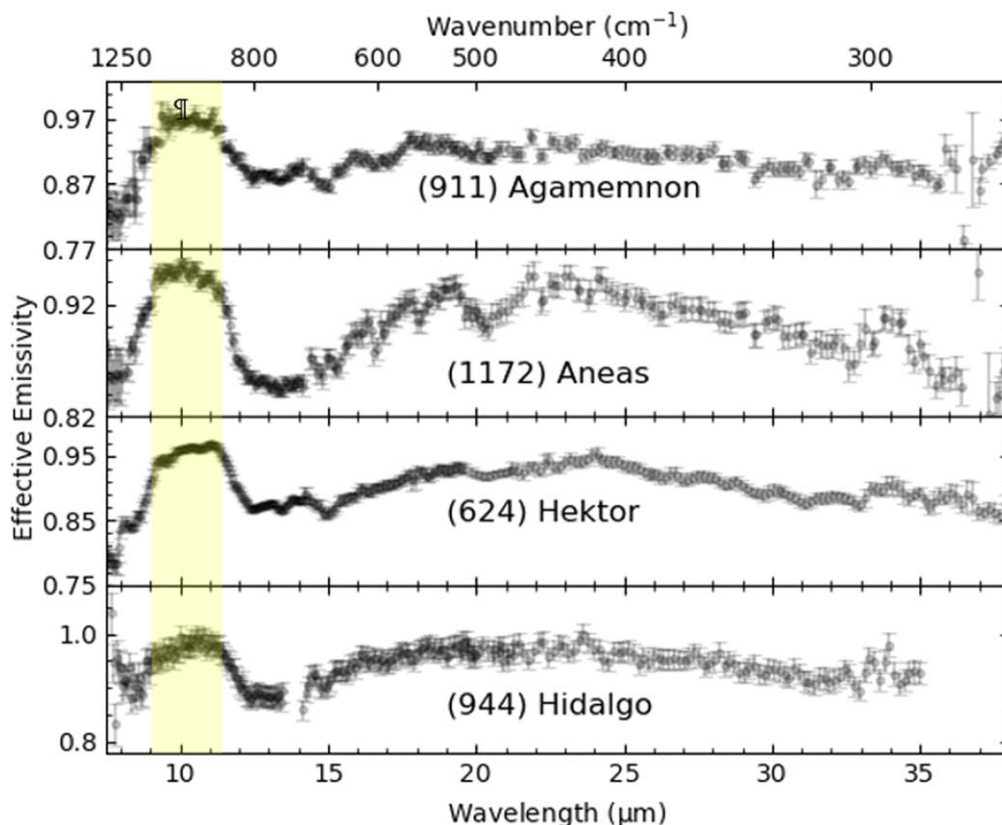


Figure 1. Emissivity spectra of Trojan asteroids (911) Agamemnon, (1172) Aneas, and (624) Hektor from Emery et al. (2006) and primitive asteroid (944) Hidalgo from Campins (2006) over the ~ 7.5 – 37.5 μm region showcasing the prominent 10 μm plateau (emphasized in yellow) in each of the spectra.

called the Lagrange points (Emery et al. 2006). Asteroids (911) Agamemnon and (624) Hektor reside in the L4 Lagrange point and exhibit a more square-shaped plateau region. On the other hand, (1172) Aneas is in the L5 Lagrange point and shows a more rounded plateau (Figure 1). To explain the spectral similarities between asteroids and comets, previous modeling investigations have been performed of (624) Hektor’s spectrum. Emery et al. (2006) applied a linear deconvolution algorithm to compare (624) Hektor’s spectrum to ASU and ASTER lab spectra of olivine (Mg-rich olivine) and enstatite (Mg-rich pyroxene) at the <75 μm particle size. Yang et al. (2013) used Hapke to model (624) Hektor’s spectrum with 5 weight % nanophase iron and 5 weight % Mg-rich olivine (≤ 2 μm particle size) suspended in a 90 weight % halite matrix (Izawa et al. 2021). Vernazza et al. (2012) implemented a spectral decomposition model commonly used to model protoplanetary disks and cometary spectra to model (624) Hektor’s spectrum, and their best fit was with a 0.1 – 10 μm particle size amorphous and crystalline olivine with some pyroxene. The remaining Trojan asteroids, (911) Agamemnon and (1172) Aneas, and primitive asteroid (944) Hidalgo have not been previously modeled. Furthermore, to our knowledge, (624) Hektor’s spectrum has not been modeled with as much depth as this study, where we have varied porosities and particle sizes.

Here we present the modeling results of the TIR spectra of the Trojan asteroids and (944) Hidalgo. The aim of this work is to better characterize the primitive asteroid regolith by modeling the prominent 10 μm plateau in their spectra. To accomplish this, we used the light-scattering multiple sphere T-matrix (MSTM) method (Mackowski & Mischenko 1996, 2011; Mackowski 2013)

and Hapke reflectance models (Hapke 2012). Similar to Emery et al. (2006) and Yang et al. (2013), we hypothesize that fine particulate olivine (<10 μm) with high porosities can explain the 10 μm spectral feature. In this study, we model the Trojan asteroids and (944) Hidalgo using porosities of 70%, 80%, 90%, and 95% and fine particles with radii of 0.1, 0.5, 1.0, and 5.0 μm .

2. Data and Computational Methods

2.1. Near-Earth Asteroid Thermal Model

The spectral energy distributions (SEDs) of Trojan asteroids (911) Agamemnon, (1172) Aneas, and (624) Hektor (panels (a), (c), and (e) in Figure 2) were obtained by Emery et al. (2006) using the Infrared Spectrograph (IRS) on the Spitzer Space Telescope. Asteroid (911) Agamemnon was observed on 2004 August 8 at 19.354 7 UT, (1172) Aneas on 2004 March 24 at 8.753 9 UT, and (624) Hektor on 2004 March 2 at 3.363 9 UT (Emery et al. 2006). All observations were done using the low spectral resolution mode ($R = \Delta\lambda/\lambda \sim 64$ – 128) spanning the 5.2 – 38 μm wavelength range split into four separate spectral segments (Emery et al. 2006). See Houck et al. (2004) for more information about the operational modes of the IRS instrument.⁵

We obtained the (944) Hidalgo SED (panel (g) in Figure 2) using the Spitzer IRS instrument. Spectra from 10 separate epochs were taken over a period of 11.3 hr centered on 2006 July 24 at 10:52 UTC. The observations used the low-

⁵ We used Dr. Joshua P. Emery’s SEDs sent directly via email communication on 2020 November 6 that he reduced using the SPICE tool with the Spitzer IRS pipeline (version S12.0).

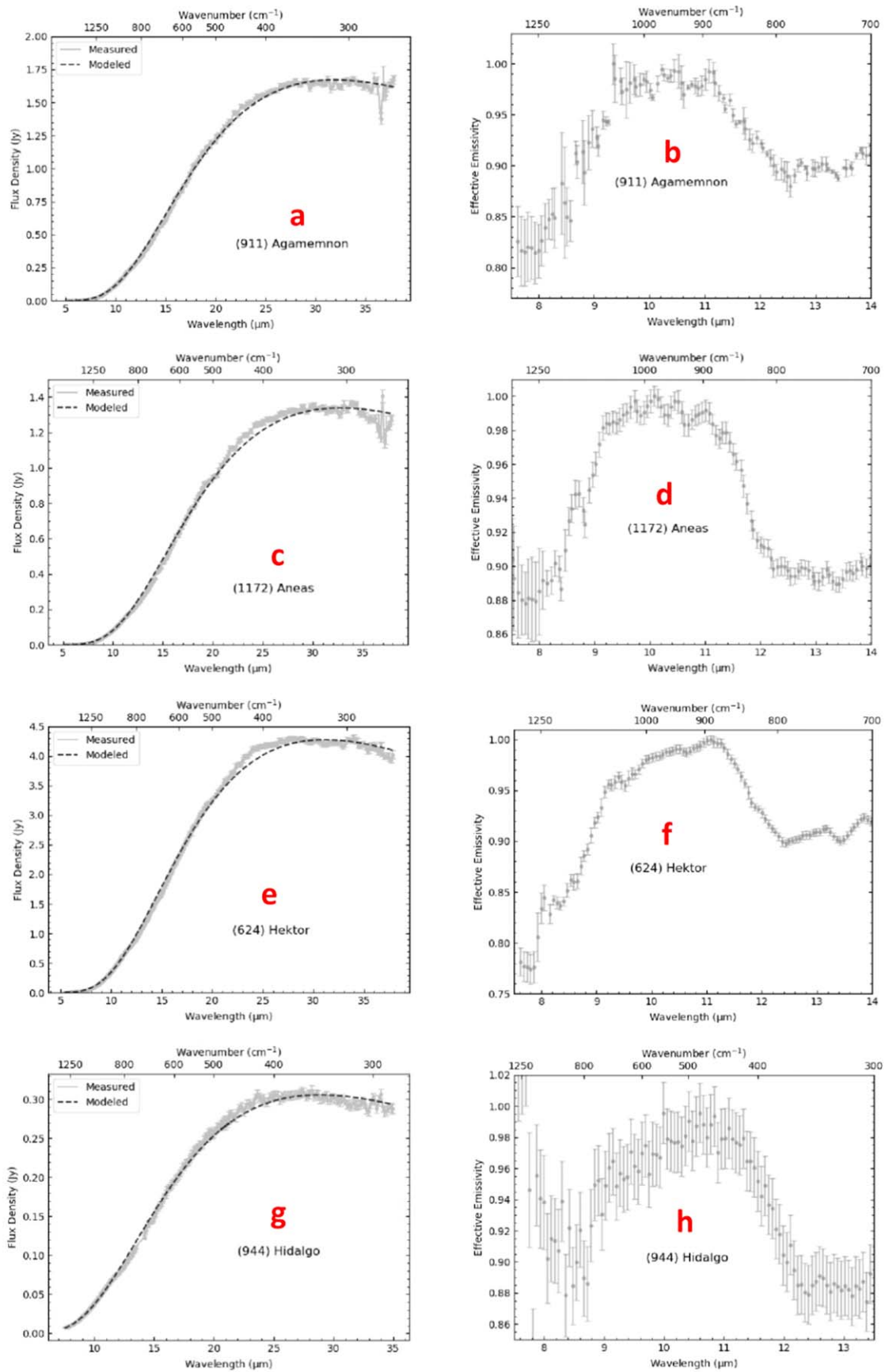


Figure 2. The best-fit NEATM SED is shown in panels (a), (c), and (e) for the Trojan asteroids, and (944) Hidalgo is shown in panel (g). Panels (b), (d), (f), and (h) show the $\sim 7.5\text{--}13.5\ \mu\text{m}$ portion of the emissivity spectrum used in the MSTM and Hapke modeling.

Table 1
NEATM Best-fit Parameters

Asteroid	H_v	p_v	η	G	r (au)	Δ (au)	α (deg)
(911) Agamemnon	7.89	$0.061^{+0.024}_{-0.019}$	0.87 ± 0.02	0.15	5.59	5.27	10.28
(1172) Aneas	8.33	$0.044^{+0.020}_{-0.014}$	0.93 ± 0.04	0.15	5.72	5.43	9.83
(624) Hektor	7.49	$0.037^{+0.028}_{-0.017}$	0.93 ± 0.02	0.15	5.19	5.23	10.96
(944) Hidalgo	10.69	$0.040^{+0.02}_{-0.01}$	$0.79^{+0.11}_{-0.19}$	0.15	4.82	4.83	12.10

Note. Here H_v is the absolute magnitude, p_v is the visual albedo (determined by χ^2 minimization), η is the asteroid beaming parameter (determined by χ^2 minimization), G is the slope parameter, r is the asteroid–Sun distance, Δ is the asteroid–observer distance, and α is the phase angle.

References. (1) See Tables 1 and 2 of Emery et al. (2006) for Trojan asteroid parameters; (2) See JPL Small-Body Database Browser 2021 for (944) Hidalgo parameters.

resolution module ($R = \Delta\lambda/\lambda \sim 60\text{--}130$) spanning the wavelengths $7.5\text{--}40\ \mu\text{m}$ in four separate spectral segments (“spectral orders” in IRS terminology). We extracted spectra from pipeline-processed data products (version S18.18.0) using the SPICE tool. Each of the extracted spectral orders (40 spectra each, 587 s exposure time) were scaled to the median flux density and averaged together, primarily to account for rotational variability but also misalignment between the slits and asteroid position. A potential artifact known as the “teardrop” (Spitzer Science Center 2012) was avoided by removing the $13.5\text{--}14.3\ \mu\text{m}$ region from the shortest order in our data set. Small discontinuities remained between spectral orders. We therefore extrapolated neighboring spectral orders to a common wavelength to derive order-to-order scaling factors and produce a near-continuous spectrum. The largest correction was 6%.

To determine the emissivity spectra from the SEDs, we fit a modeled SED, which is essentially a blackbody spectrum, to each asteroid SED using C++ code written by Mueller (2018) based on the Near-Earth Asteroid Thermal Model (NEATM; Harris 1998) and using the same NEATM parameters (H_v , G , r , Δ , and α) as Emery et al. (2006; see Table 1). The optimal fit of the modeled SED to the asteroid SED for each asteroid was achieved by adding a χ^2 minimization routine to the Mueller (2018) code to iterate over values within the uncertainties of p_v and η . Note that the uncertainties provided in Table 1 for (944) Hidalgo are only the values we iterated in between for p_v and η . They are not uncertainties in the values of p_v and η . This is because we obtained the values (H_v , G , r , Δ , and α) for (944) Hidalgo from the JPL Small-Body Database Browser 2021, and there are no uncertainties associated with the values. We then divided the asteroid SED by the modeled SED to obtain the emissivity spectrum for each asteroid shown in Figure 2. The NEATM fit for each asteroid was over the TIR ($\sim 5\text{--}38\ \mu\text{m}$). We have restricted the MSTM and Hapke modeling to the wavelength region around $\sim 7.5\text{--}13.5\ \mu\text{m}$ shown in panels (b), (d), (f), and (h) in Figure 2 because the $10\ \mu\text{m}$ plateau region is the most prominent spectral feature of the asteroid spectra (Figure 1).

2.2. MSTM

The FORTRAN-90 MSTM method (Mackowski & Mishchenko 1996, 2011; Mackowski 2013) is a light-scattering model used to optically characterize particulate media (Ito et al. 2017, 2018). It computes the electromagnetic radiation interaction between many particles, making it useful in modeling asteroid regolith (Ito et al. 2017). In the TIR, volumetric scattering becomes a problem when the particle size is

comparable to the wavelength of light around $<25\ \mu\text{m}$, and this problem intensifies as the particle size decreases (Ramsey & Christensen 1998). However, MSTM can handle light scattering between particles of this size and wavelength regime, making it ideal for modeling fine particulate regolith (Ito et al. 2017, 2018).

The computations were performed on the Stokes High Performance Computing cluster at the University of Central Florida (Stokes 1992). Target parameters such as the particle positions, size parameter ($2\pi r/\lambda$, where r is the particle radius and λ is the wavelength of light), and principal indices of refraction of each mineral in Table 2 are required inputs (Ito et al. 2017, 2018). In light-scattering models like the MSTM, optical constants, i.e., the complex index of refraction, represent the composition of a material and thus an essential input for modeling spectra. The complex indices of refraction were specified at each wavelength channel (100 channels) over the $\sim 7.5\text{--}13.5\ \mu\text{m}$ wavelength range. To improve the accuracy in the final MSTM and Hapke modeled spectrum, the contribution of each of the three crystallographic axes to the emissivity spectrum of fayalite and forsterite are calculated in Section 2.2.1. Additional user-specified parameters for MSTM may be found in the Appendix. The minerals in Table 2 were chosen for modeling based on those present in comet Hale-Bopp, C03 carbonaceous chondrite meteorites, and CY chondrite meteorites, which show a prominent $10\ \mu\text{m}$ feature in their spectra (Crovisier et al. 2000; Emery et al. 2006; Bates et al. 2021). These planetary bodies are composed of silicates, mainly olivine and pyroxene, with minor amounts of other silicates, including phyllosilicates, sulfides, and carbonates (Brearley & Jones 1998, pp. 313–398; Crovisier et al. 2000; Bates et al. 2021). The particle positions and radii were specified using a Python script we wrote that generates the x , y , and z coordinates of each monodispersed, spherical particle in a rectangular prism (the size of the prism was based on the assumption that $\rho V_m = nV_p$, where ρ is the packing density, V_m is the volume of the whole medium, n is the number of particles, and V_p is the volume of particles). For example, a rectangular prism with $n = 200$ particles of a $0.5\ \mu\text{m}$ radius size and 70% porosity would have a volume of $V_m = 350\ \mu\text{m}^3$. A single rectangular prism containing all of the particles was used for a single model run. For example, if only olivine was modeled, then the particles in the rectangular prism would be all olivine for a single model run. Likewise, if a mixture of several minerals was modeled, then the rectangular prism would contain all of the minerals at their chosen abundances for a single model run.

Table 2
Summary of Particle Sizes and Chemical Formulae for MSTM and Hapke Modeled Minerals

Modeled Mineral (Reference)	Chemical Formula	Particle Sizes (μm)			
Forsterite (1)	Mg_2SiO_4	0.1	0.5	1.0	5.0
Fayalite (1)	Fe_2SiO_4	0.1	0.5	1.0	5.0
Enstatite (1)	MgSiO_3	0.1	0.5	1.0	5.0
Amorphous pyroxene (1)	$\text{Mg}_{0.95}\text{Fe}_{0.05}\text{SiO}_3$		0.5		5.0
Amorphous pyroxene (1)	$\text{Mg}_{0.8}\text{Fe}_{0.2}\text{SiO}_3$		0.5		5.0
Amorphous pyroxene (1)	$\text{Mg}_{0.6}\text{Fe}_{0.4}\text{SiO}_3$		0.5		5.0
Amorphous pyroxene (1)	$\text{Mg}_{0.5}\text{Fe}_{0.43}\text{Ca}_{0.03}\text{Al}_{0.04}\text{SiO}_3$		0.5		5.0
Amorphous pyroxene (1)	$\text{Mg}_{0.4}\text{Fe}_{0.6}\text{SiO}_3$		0.5		5.0
Amorphous olivine (1)	$\text{Mg}_{0.8}\text{Fe}_{1.2}\text{SiO}_4$		0.5		5.0
Amorphous enstatite (2)	MgSiO_3		0.5		5.0
Amorphous forsterite (2)	Mg_2SiO_4		0.5		
Troilite (3)	FeS		0.5		
Calcite (1)	CaCO_3		0.5		
Muscovite mica (4)	$\text{Al}_2\text{K}_2\text{O}_6\text{Si}$		0.5		
Orthopyroxene (5)	$\text{Mg}_2\text{Si}_2\text{O}_6$		0.5		
Kaolinite (5)	$\text{Al}_2\text{Si}_2\text{O}_5(\text{OH})_4$		0.5		
Serpentine (5)	$\text{C}_{21}\text{H}_{21}\text{N}_2\text{O}_3^+$		0.5		
Pyrophyllite (5)	$\text{Al}_2\text{Si}_4\text{O}_{10}(\text{OH})_2$		0.5		
Montmorillonite (5)	$\text{Al}_2\text{H}_2\text{O}_{12}\text{Si}_4$		0.5		
Saponite (5)	$\text{Al}_4\text{H}_{12}\text{Mg}_{18}\text{O}_{72}\text{Si}_{21}$		0.5		
Palagonite (5)	Pahala ash from the beach at South Point, Hawaii; see Bartholomew & Crisp (1989) and Roush et al. (1991)		0.5		
Halite (6)	NaCl		0.5		

References. (1) <https://www.astro.uni-jena.de/Laboratory/OCDB/crsilicates.html>; (2) Scott & Duley (1996), (3) Henning & Stognienko (1996), (4) Singleton & Shirkey (1983), (5) Roush et al. (1991), (6) T. Glotch 2021, personal communication.

Initially, we modeled each mineral at the $0.5 \mu\text{m}$ radius size. We used ~ 200 – 300 nonoverlapping particles (to avoid strange transmission effects when k is low). There are two main parameters that affect the computational time. One is the size parameter (ratio of the particle radius to the wavelength of light), so the code will take longer to run at short wavelengths (where the particle size/wavelength ratio is larger) than at longer wavelengths. The other parameter that increases the computational time is whether MSTM is run in fixed or random orientation of light (see the Appendix for more details). A rectangular prism of 200 – 300 particles at the $0.5 \mu\text{m}$ radius size (random orientation) may take a few hours to run. But a rectangular prism with the same number of particles at the $5 \mu\text{m}$ radius size can take up to ~ 100 days to run in the random orientation. Output by MSTM consists of the extinction and scattering efficiencies, Q_{ext} and Q_{sca} , at each wavelength channel. The ratio of these efficiencies is the single-scattering albedo, which is a required input for the Hapke model. Furthermore, the single particle phase function describes the scattering of power by a particle (Hapke 2012) and is also output by MSTM and required for input in Hapke.

Each mineral's modeled emissivity spectrum was plotted against the asteroid spectra for comparison. All minerals were initially modeled at the $0.5 \mu\text{m}$ particle size, but for modeled minerals showing the lowest rms errors (e.g., forsterite, fayalite, and enstatite), we modeled additional particle radius sizes of 0.1 , 1.0 , and $5.0 \mu\text{m}$ to improve the model fit from the $0.5 \mu\text{m}$ particle size. Bulk porosities (volume ratio of void space to particles in a single rectangular prism) of 70% , 80% , 90% , and 95% were modeled for each mineral to determine the best fit to the asteroid spectra and test whether high porosities like those in cometary comae were necessary to get the best fit (Emery et al. 2006; Rivkin et al. 2009; Yang et al. 2013).

2.2.1. Complex Indices of Refraction Weights

The complex indices of refraction n (n_x , n_y , n_z) and k (k_x , k_y , k_z) for fayalite (Fe-rich olivine) and forsterite (Mg-rich olivine) are plotted in the top and middle panels of Figures 3 and 4. Their complex indices of refraction have x , y , and z contributions because they are crystal minerals that possess three crystallographic axes. We calculated a spectrum using the n and k complex indices of refraction and compared the results to the measured coarse particulate emissivity spectra of fayalite and forsterite with the following method based on Glotch et al. (2006). First, the laboratory spectra of fayalite (710 – $1000 \mu\text{m}$ particle size fraction) and forsterite (San Carlos olivine, 250 – $500 \mu\text{m}$ particle size fraction) were obtained from the Arizona State University (ASU) spectral library (Christensen et al. 2000) and the Planetary Analog Surface Chamber for Asteroid and Lunar Environments at the University of Oxford (Donaldson Hanna & Bowles 2020), respectively. These spectra are plotted in the bottom panels of Figures 3 and 4. The Fresnel equations, which describe the reflection and transmission of an electromagnetic wave by a plane boundary (Hapke 2012), are used to produce a reflectance spectrum for each complex index of refraction. The reflectance spectrum is inverted to emissivity using Kirchhoff's law ($E = 1 - R$, where R is reflectance). For example, if we input the x contribution complex index of refraction (e.g., n_x and k_x) into the Fresnel equations, we retrieve the x contribution to the emissivity spectrum (E_x). We then repeat this process using the y (e.g., n_y and k_y) and z (e.g., n_z and k_z) complex indices of refraction to obtain the y and z contribution to the emissivity spectrum, or E_y and E_z . With this spectral library of E_x , E_y , and E_z and a weighted least-squares (WLS) linear model, we fit the coarse laboratory spectra. The WLS linear model is appropriate for coarse particle spectra (surface scattering dominates) because

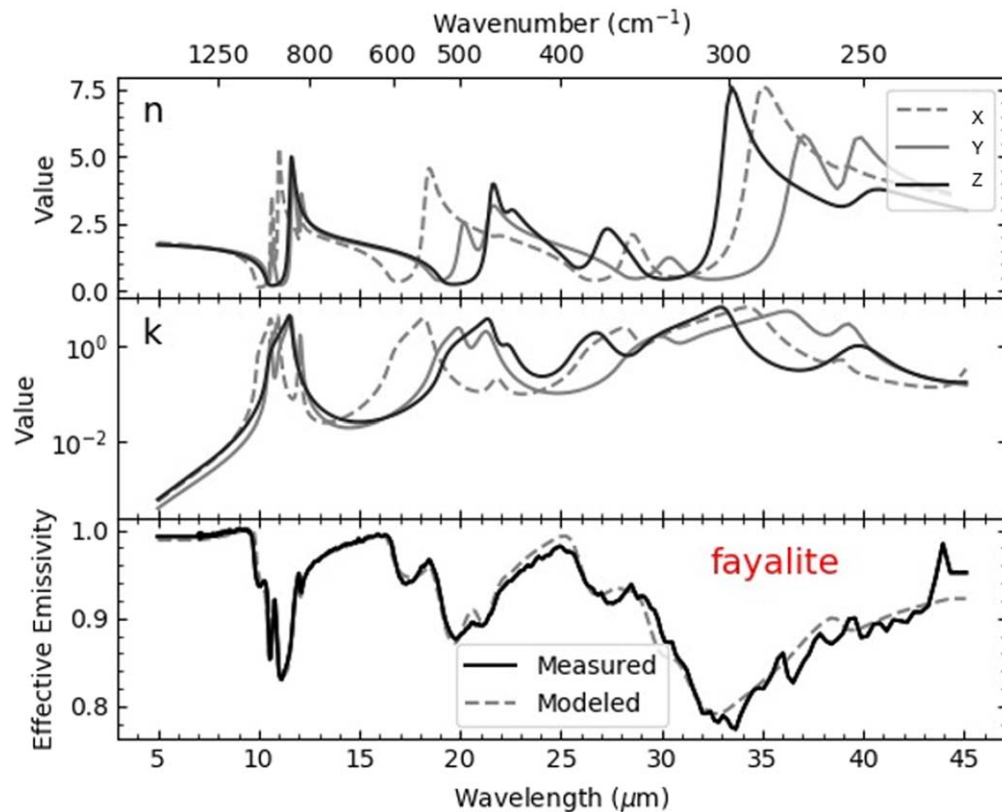


Figure 3. Fayalite complex indices of refraction n and k are shown in the top and middle panels. The ASU laboratory fayalite spectrum is shown in the bottom panel (Christensen et al. 2000; solid curve). The modeled spectrum (bottom panel, dashed curve) is plotted with weight contributions of (39.5%, 31.0%, 29.4%) for (A, B, C), respectively.

the particle sizes are large compared to the wavelength of light (Ramsey & Christensen 1998; Rogers & Aharonson 2008). We also minimized the rms error in the WLS model fit with respect to the angle of incident light, θ , in the Fresnel equations by iterating θ from 0° to 90° in 1° increments. We performed the angle-of-light minimization to obtain the best fit to the laboratory spectra and because emissivity spectra are independent of the angle of incident light. Finally, the WLS retrieved abundances (blackbody normalized) are the weight contributions of each of the three complex indices of refraction (referred to as A, B, and C in Table 2 and Figures 3 and 4). For example, in Table 3, for fayalite, the best fit obtained in the bottom panel of Figure 3 would have weights of 39.5%, 31.0%, and 29.4% (Table 3) for A, B, and C, respectively. So, the emissivity spectrum shown in the bottom panel of Figure 3 (labeled as modeled; dashed line) is reproduced by $E = A E_x + B E_y + C E_z = 0.395 E_x + 0.31 E_y + 0.294 E_z$. This method using the Fresnel equations and WLS linear model was used to determine the weights of the complex indices of refraction (Table 3) for both fayalite and forsterite (see Figures 3 and 4).

2.3. Hapke Reflectance Model

Following the calculation of the scattering parameters by MSTM, the isotropic multiple-scattering approximation model, a widely used equation in planetary science to study light reflected from planetary bodies, was used to approximate bidirectional reflectance (Hapke 2012). The Hapke model is needed after MSTM modeling because the scattering parameters that MSTM outputs must be input to Hapke to obtain a

reflectance spectrum that we invert to emissivity. It is given by (Equation (8.60) in Hapke 2012)

$$r(\mu, \mu_o, \alpha) = \frac{w}{4\pi} \frac{\mu_o}{\mu_o + \mu} [p(\alpha) + H(\mu)H(\mu_o) - 1]. \quad (1)$$

The single-scattering albedo, w , in Equation (1) is found by dividing the extinction efficiency Q_{ext} by the scattering efficiency Q_{sca} , which are output by MSTM. Additional output by MSTM includes the single particle phase function $p(\alpha)$. We extract the corresponding $p(\alpha)$ from the MSTM output based on the phase angle α from Table 1. The variables μ and μ_o in Equation (1) are the cosines of the reflection and incidence angles, respectively. The $H(\mu_o)$ and $H(\mu)$ in Equation (1) are the Ambartsumian–Chandrasekhar H function (Equation (8.53) in Hapke 2012), approximated by

$$H(\mu) \cong \frac{1 + 2\mu}{1 + 2\mu} \quad (2)$$

and

$$H(\mu_o) \cong \frac{1 + 2\mu_o}{1 + 2\mu_o}. \quad (3)$$

Python code written by Dr. Jessica Arnold (J. Arnold, personal communication, 2020 July 17) that computes Equations (1), (2) and (3) and implements the miepython module⁶ was used to determine the Hapke bidirectional reflectance. After the calculation of the bidirectional reflectance, the modeled emissivity spectrum for a single mineral is obtained by

⁶ https://miepython.readthedocs.io/en/latest/03_angular_scattering.html

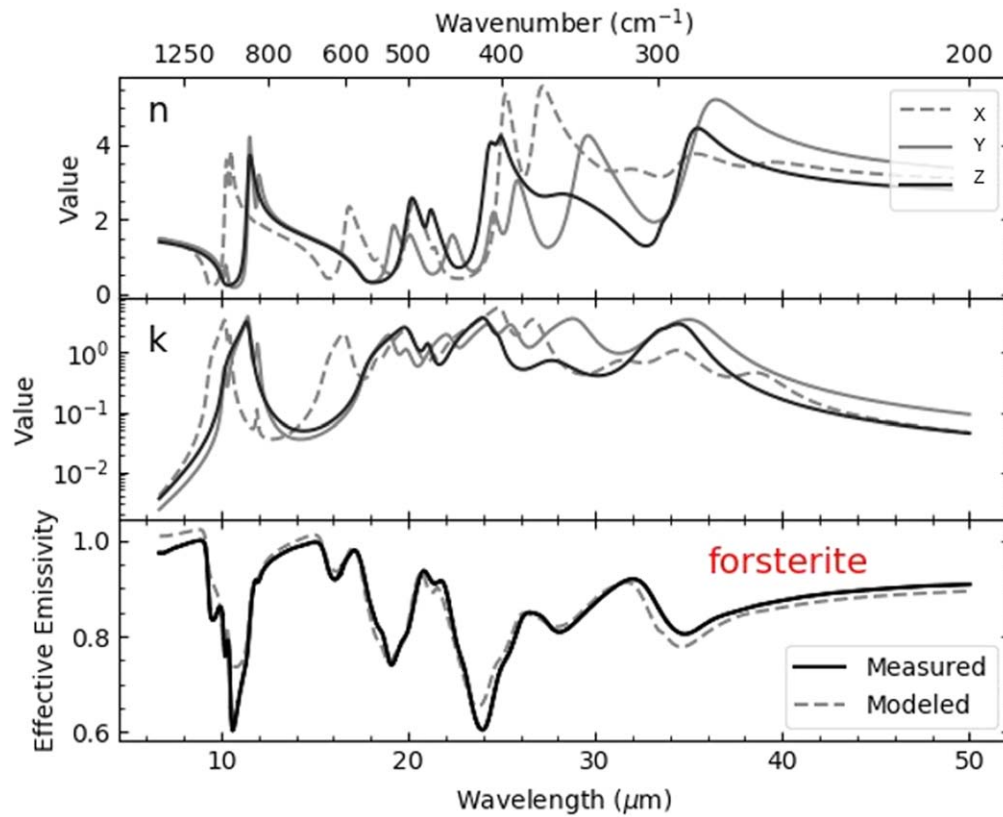


Figure 4. Forsterite complex indices of refraction n and k are shown in the top and middle panels. The Oxford laboratory forsterite spectrum is plotted in the bottom panel (Donaldson Hanna & Bowles 2020; solid curve). The modeled spectrum is plotted with weight contributions of (41.6%, 32.6%, 25.8%) for (A, B, C), respectively (bottom panel, dashed curve).

Table 3

Measured Olivine Particle Sizes, Angle of Incident Light θ Chosen to Minimize the rms Error in the WLS Fit, and Complex Indices of Refraction Weights (A, B, C)

Mineral	Particle Sizes (μm)	θ (deg)	A (%)	B (%)	C (%)
Forsterite	250–500	31	41.6	32.6	25.8
Fayalite	710–1000	0	39.5	31.0	29.4

inverting the reflectance using Kirchhoff’s law ($E = 1 - R$, where E is the emissivity and R is the reflectance).

2.4. WLS Method

The MSTM and Hapke modeled emissivity spectra for individual minerals were combined linearly using a WLS model. The WLS model is only used to narrow down possible parameters, such as the number of end-members in the spectral library, and porosities to reduce the number of model iterations and thus computational time needed to find the lowest rms error (best model fit). Without using the WLS model, we would have had to search through more parameter space to find the best model fit. To start, the minerals from Table 2 were modeled individually to produce a single emissivity spectrum (e.g., a forsterite spectrum at 100% abundance was modeled at a single particle size and porosity) using MSTM and Hapke. Next, the individually modeled minerals were then used as end-members in a spectral library supplied to the WLS model to fit an asteroid spectrum. However, the mineral abundances, particle sizes, and porosities obtained using the WLS were only used as

starting points for the computation of the final TIR spectral method discussed in Section 2.5. This is because the WLS linear model does not accurately model fine particulate ($<10 \mu\text{m}$) emissivity spectra due to the nonlinear mixing that occurs across TIR wavelengths (Lowry et al. 2022). Despite this inaccuracy, the WLS method aided in narrowing down the number of possible particle sizes, porosities, and minerals needed to model each asteroid spectrum using the final method. The WLS-computed abundance uncertainties arise from the uncertainties associated with each asteroid’s measured spectrum. The minerals being modeled by WLS are fit to the asteroid spectrum, but since we have uncertainty bars on each asteroid spectrum, this leads to a degree of uncertainty in the computed abundances. The results of the WLS method are found in Section 3.1. A summary of this method can be found in steps 1, 2, and 3 in Figure 5.

2.5. Computation of the Final TIR Spectral Method

Following the WLS method outlined in Section 2.4, and to obtain the final fit, we used the abundances derived from the WLS modeling as input into the MSTM and Hapke models. So, the computation of the final TIR spectral method is a continuation of the WLS method described in Section 2.4. The mineral abundances derived from WLS are the most likely minerals (particle sizes and porosity) to fit the spectrum. We began by specifying the particles sizes (shown in Table 4) and optical constants in the MSTM input for each particle. Other information included in the MSTM input files was the bulk porosity, which we determined by averaging the fifth column in Table 4 for each asteroid. For example, the WLS method

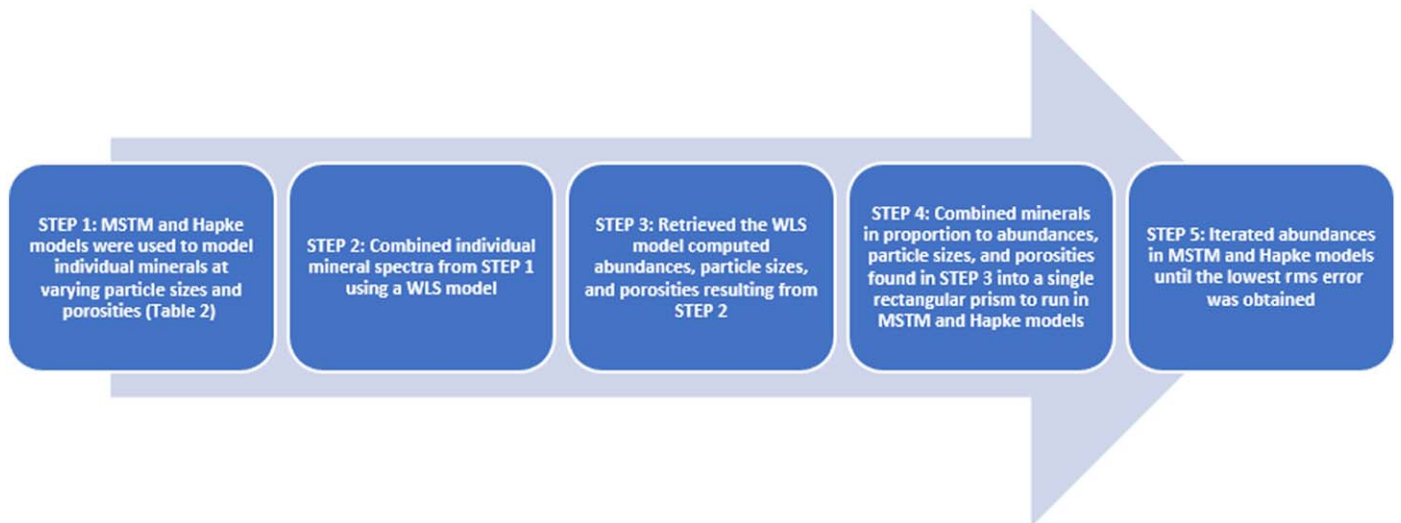


Figure 5. Summary of the full methodology outlined in Sections 2.4 and 2.5. Note that steps 4 and 5 do not use the WLS model.

Table 4
WLS Method Modeled Abundances (volume %)

Asteroid	Particle Size (μm)	Mineral	Abundances (volume %)	Porosity (%)	rms Error
(911) Agamemnon	0.5	Fayalite	54 ± 2	70	1.09E-02
	0.5	Forsterite	46 ± 2	80	
(1172) Aneas	1.0	Fayalite	37 ± 2	90	1.15E-02
	1.0	Forsterite	37 ± 3	80	
	0.5	Troilite	26 ± 1	70	
(624) Hektor	0.5	Fayalite	73 ± 1	70	1.03E-02
	0.5	Forsterite	26 ± 1	70	
(944) Hidalgo	0.5	Fayalite	45 ± 14	70	2.06E-02
	0.5	Forsterite	35 ± 22	50	
	0.5	Troilite	19 ± 11	95	

retrieved fayalite and forsterite at porosities of 70% and 80% (fifth column of Table 4), respectively, which were then averaged to give a resulting 75% (average of fifth column of Table 4 for (911) Agamemnon) set by specifying the xyz positions of each particle in MSTM (a more detailed description is in Section 2.2). To represent the computed WLS abundances for (911) Agamemnon, 54% by volume of the 0.5 μm size particles were set to fayalite, and 46% by volume of the same particle size were set to forsterite. We did not iterate over bulk porosities in this method to limit the number of free variables.

Following output by MSTM of the scattering efficiency, extinction efficiency, and single particle phase function, the Hapke model was run using the scattering parameters computed by MSTM for each iteration. Multiple iterations of MSTM and Hapke were performed by adjusting the mineral abundances by $\pm 5\%$ by volume (always summing to 100%) while porosity was held constant to find the minimum rms error between the model and each asteroid spectrum. For example, we started modeling 54% by volume fayalite and 46% by volume forsterite to fit the (944) Agamemnon spectrum. In the next iteration, we adjusted the abundances to 59% by volume fayalite and 41% by volume forsterite. We repeated this process of adjusting the abundances while we observed the rms error decreasing. So, in the case of (911) Agamemnon, we continued

to increase the volume percentage of fayalite (decreasing the volume percentage of forsterite), since we observed the rms error decreasing and found that the lowest rms error was by modeling 100% by volume fayalite (Table 5). Note that the abundance uncertainties computed by WLS were considered during iteration of the models by iterating within the uncertainty values. The rms error that quantifies the goodness of fit for a single model iteration is given by

$$\text{rms} = \sqrt{\sum_{j=1}^m \frac{\delta(\lambda)_j^2}{m}},$$

where m is the number of wavenumbers, and $\delta(\lambda)$ is the residual error (difference between the modeled and measured spectrum). This process resulted in our final fits discussed in Section 3.2, with the rms errors located under the asteroid name in each plot and in the last column of the tables. A summary of this method is shown in steps 3, 4, and 5 of Figure 5.

3. Results

3.1. WLS Method

The modeled mineral abundances, uncertainties, and fit are shown in Table 4 and Figure 6. The WLS model fit a higher abundance of fayalite than forsterite to the (911) Agamemnon,

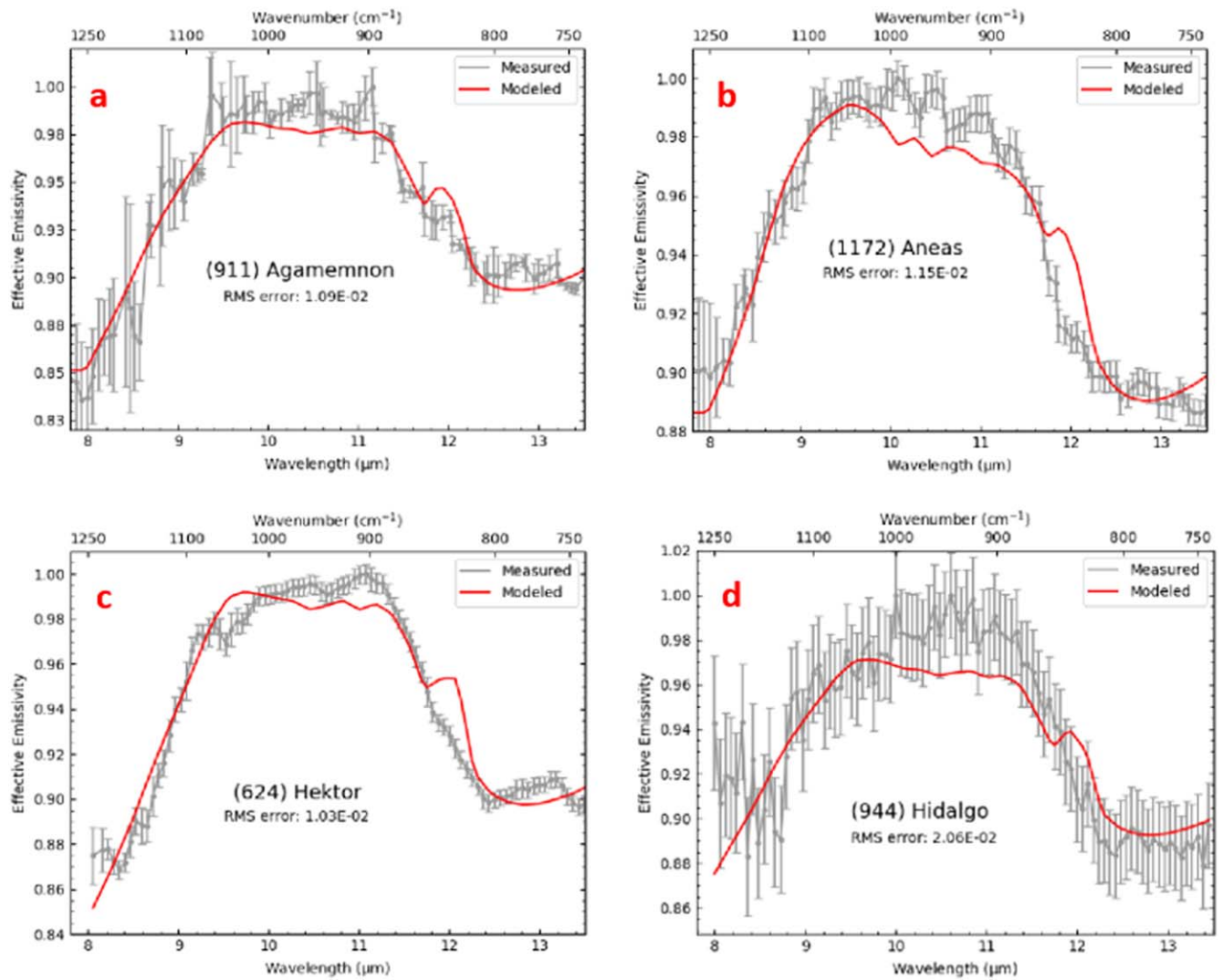


Figure 6. The WLS model fits (red lines) to Trojan and (944) Hidalgo spectra (gray lines) corresponding to Table 4.

Table 5
Final Method Modeled Abundances

Asteroid	Particle Size (μm)	Mineral	Abundance (volume %)	Bulk Porosity (%)	rms Error
(911) Agamemnon	0.5	Fayalite	100	75	1.35E-02
(1172) Aneas	1.0	Fayalite	49	80	1.67E-02
	1.0	Forsterite	33		
	0.5	Troilite	18		
(624) Hektor	0.5	Fayalite	100	70	2.58E-02
(944) Hidalgo	1.0	Fayalite	48	70	1.93E-02
	1.0	Forsterite	48		
	1.0	Troilite	4		

(1172) Aneas, and (944) Hidalgo spectra. Fayalite and forsterite were both fit to the (624) Hektor spectrum, with a higher abundance of fayalite than forsterite. Additionally, the WLS fit the spectrally flat end-member troilite to the (1172) Aneas and (944) Hidalgo spectra to lower the spectral contrast of the $10\ \mu\text{m}$ plateau in the modeled spectrum. Mineral porosities ranged from 50% to 95% with particle sizes of either 0.5 or $1.0\ \mu\text{m}$ for all model fits.

The model fit to the spectra for the Trojans in Figures 6(a), (b), and (c) are within most of the uncertainty bars, but near

$12\ \mu\text{m}$, there is an obvious difference observed between the measured and modeled spectra: an emissivity peak, due to the crystalline nature of olivine (versus amorphous olivine), in the model that is not observed in the measured spectra. The mismatch is not as pronounced in the (911) Agamemnon spectrum fit as it is in the other asteroids. An additional discrepancy is observed from ~ 10 to $11\ \mu\text{m}$ in the (1172) Aneas spectrum fit, where there is a difference in slope between the modeled and measured spectrum; i.e., the modeled spectrum showed a more negative slope in this wavelength

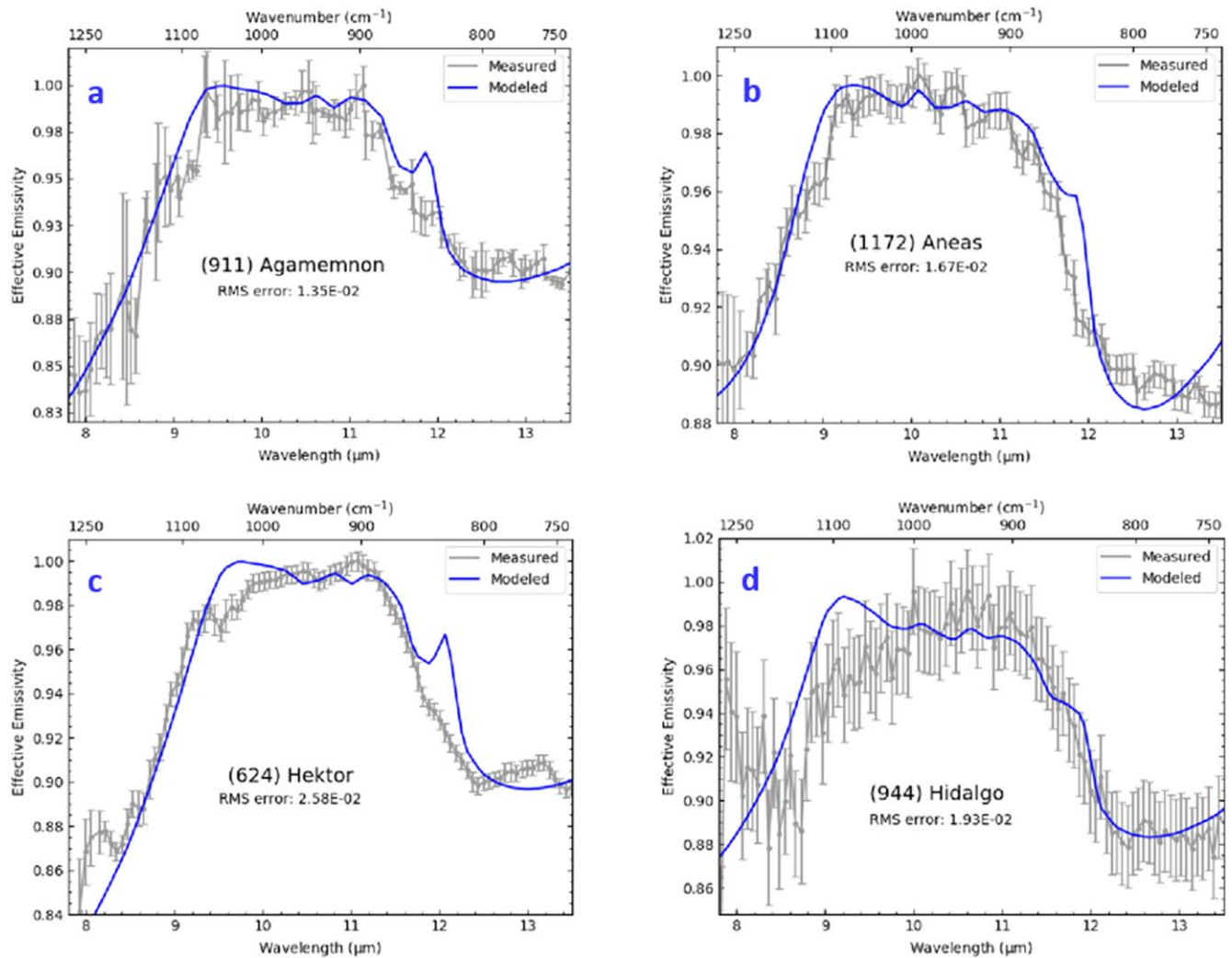


Figure 7. The MSTM and Hapke method results of modeling Trojan and (944) Hidalgo spectra with the abundances shown in Table 5.

region. Furthermore, the model was fit to lower emissivity values that are outside of the uncertainty bars of the Aneas spectrum.

3.2. Computation of the Final TIR Spectra Results

The results for the abundances derived from MSTM and Hapke modeling are shown in Table 5, and the resulting model fits are in Figure 7. The (911) Agamemnon and (1172) Aneas spectra had the best model fits or lowest rms errors. We fit 100% fayalite to (911) Agamemnon to obtain the lowest rms error, while the (1172) Aneas spectrum required fayalite, forsterite, and troilite to obtain the lowest rms error. The Trojan model fits (Figures 7(a), (b), and (c)) show a difference between the measured and modeled spectra near $12\ \mu\text{m}$ resulting from a peak in emissivity in the model that is not seen in the measured spectra. The crystalline nature of olivine versus amorphous is what causes the peak in emissivity observed in the modeled spectrum. This mismatch is most pronounced in the (624) Hektor spectrum, and it is least pronounced in (1172) Aneas. Furthermore, the largest differences and rms errors between modeled and measured spectra were observed in (624) Hektor. Multiple portions of the modeled spectrum, including $\sim 8\text{--}8.4$, $\sim 9\text{--}10.2$, ~ 11 , and $\sim 12\text{--}13\ \mu\text{m}$, were outside of the uncertainty bars of the (624)

Hektor spectrum. Note that the (944) Hidalgo uncertainty bars in the spectrum were large with respect to the spectral features, so that the model fit is not unique; many different abundances of minerals could possibly have shown a similar fit but not have the lowest rms error, as seen in Figure 7(d). The bulk porosities for the final fits were between 70% and 80% for all asteroids. This range of porosities is comparable to the lunar-like porosities present in the lunar regolith that may range from $\sim 74\%$ to 87% (Hapke & Sato 2016).

4. Discussion

In this study, we modeled primitive asteroid spectra using the light-scattering MSTM and Hapke reflectance models. To summarize, we modeled 21 crystalline and amorphous structured minerals with varied particle sizes and porosities. We found that a mixture of fine particulate (0.5 and $1.0\ \mu\text{m}$ particle sizes) olivine components (e.g., fayalite and forsterite) and sometimes troilite (\sim one to three minerals required to model each asteroid spectrum) at lunar-like porosities were required to model the $10\ \mu\text{m}$ plateau over the $\sim 7.5\text{--}13.5\ \mu\text{m}$ region of the TIR. The parameters of composition, particle sizes, and porosities required for modeling the asteroid spectra are discussed below in more detail, as are their implications.

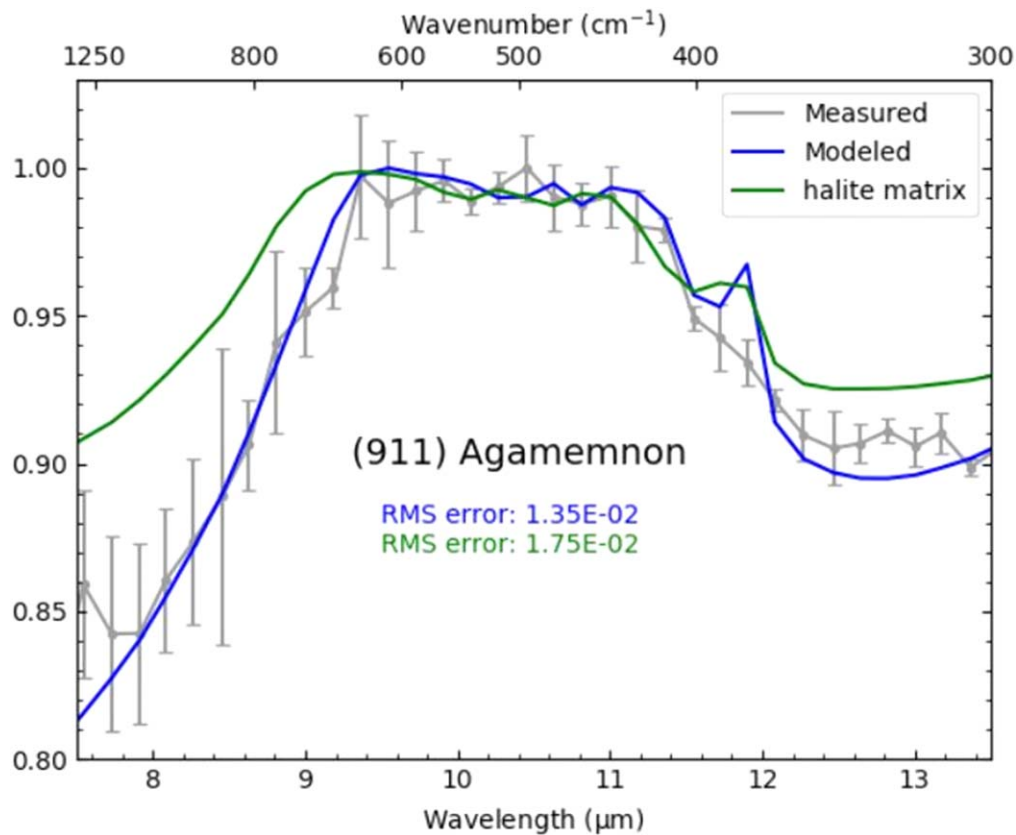


Figure 8. Asteroid (911) Agamemnon modeled using 25% by volume halite and 75% by volume fayalite (green). The modeled spectrum of 100% by volume fayalite at the $0.5 \mu\text{m}$ particle size and with a bulk porosity of 75% is shown in blue for comparison (identical to Figure 7(a)). The measured spectrum of (911) Agamemnon is shown in gray.

Martin et al. (2022), Izawa et al. (2021), Yang et al. (2013), and Emery et al. (2006) previously showed that the Trojan spectra could be modeled by spectra of fine particulate olivine embedded in a transparent matrix such as a salt (e.g., halite or potassium bromide). In Yang et al. (2013), their best fit to the (624) Hektor spectrum contained 25% by volume halite. To compare our study to Yang et al. (2013), and with the goal of obtaining the best fit to the (911) Agamemnon spectrum, we modeled 25% by volume halite with 75% by volume fayalite at the $0.5 \mu\text{m}$ particle size (Figure 8). The complex indices of refraction for halite were measured by Dr. Timothy Glotch at Stonybrook University (Glotch 2016), and they are publicly available at http://aram.ess.sunysb.edu/tglotch/optical_constants.html. This combination of halite and fayalite simulated a bulk porosity of 75%. With the addition of halite as a proxy for porosity, since it is relatively transparent in the TIR, we observed a similar fit to that without the halite but with a slightly larger rms error, since the slopes on both sides of the $10 \mu\text{m}$ plateau are better fit without it (Figure 8). So, we determined that a transparent matrix such as halite is not necessary for modeling the $\sim 7.5\text{--}13.5 \mu\text{m}$ plateau region. The modeling sufficiently reproduces porosity without having to use halite as a proxy.

Both the (911) Agamemnon and (624) Hektor spectra were fit using fayalite (Fe-rich olivine) in 100% abundance with similar bulk porosities, suggesting a possible compositional trend in the L4 Trojan population. This is not surprising due to the similar shape of their spectra; they show a square-shaped $10 \mu\text{m}$ plateau (Figure 7) compared to the more rounded plateau in the (1172) Aneas and (944) Hidalgo spectra. Similar spectral features and model results between (1172) Aneas and

(944) Hidalgo indicate that they could have formed under similar conditions in the same region of the solar nebula. To fit the (1172) Aneas and (944) Hidalgo spectra, a mixture of fayalite, forsterite, and troilite was required. Based on this result for fayalite and forsterite, we anticipate that an intermediary olivine composed of roughly equal amounts of iron and magnesium would fit these spectra (Koeppen & Hamilton 2008). For example, if the optical constants had been available, we could have begun the modeling and likely achieved a similar fit using the optical constants for an intermediary olivine instead of pure fayalite and forsterite. However, the optical constants for intermediary olivine compositions have yet to be measured.

The Trojan asteroids and (944) Hidalgo are not only qualitatively spectrally similar but also show a similar mineralogy to that of cometary comae and meteorites. The spectra of the Trojan asteroids and (944) Hidalgo have $10 \mu\text{m}$ plateaus similar to the spectra of cometary comae and carbonaceous chondrite meteorites (Emery et al. 2006), which are composed primarily of fine particulate olivine ($\sim 0.2\text{--}0.5 \mu\text{m}$; Hanner et al. 1984; Campins & Ryan 1989; Hanner et al. 1994). Our modeling results for the (624) Hektor spectrum may be compared to comet Hale-Bopp, whose spectrum is very similar in shape near $10 \mu\text{m}$ (see Figure 9 in Emery et al. 2006). Hale-Bopp's spectrum revealed the presence of crystalline Mg-rich olivine (22%; Crovisier et al. 2000) and amorphous and crystalline pyroxene (78%; Crovisier et al. 2000) at very small particle sizes (peak of $0.2 \mu\text{m}$; Emery et al. 2006). However, more recently, Harker et al. (2002, 2004) and Lisse et al. (2007) found a much higher abundance of Mg-rich olivine, $\sim 50\%$ –

60%, compared to the 22% found by Crovisier et al. (2000). The best spectral matches to the Trojan asteroid spectra to date are the CO3 and CY carbonaceous chondrites (Figure 5 in Emery et al. 2006; Figures 5(c) and (d) in Bates et al. 2021). The CO3 carbonaceous chondrite meteorites have a very fine-grained ($<0.5 \mu\text{m}$) matrix composed of anhydrous Fe-rich olivine ($<F_{a1}$ to F_{a60}), high- and low-Ca pyroxene, Fe and Ni metal, magnetite, pentlandite, pyrrhotite, anhydrite, and minor amounts of phyllosilicates (Brearley & Jones 1998, pp. 313–398). Mineralogical studies of the CY meteorites in Bates et al. (2021) showed a high abundance of olivine (Fo70) and pyroxene with up to 30% by volume Fe sulfide and minor amounts of carbonate and metal. Our modeling results, which suggest that the Trojan asteroids and Hidalgo are composed of fine particulate olivine, corroborate these published results of comet Hale-Bopp and the CO3 and CY meteorites.

Although we modeled the spectra using single particle sizes, we know that complex particle size distributions (PSDs) are present in asteroid regolith (e.g., Hörz & Cintala 1997). In this study, we are only emphasizing the spectrally dominant particle size of the PSDs present in the asteroid regolith. Since the Trojan and (944) Hidalgo spectra closely resemble those of cometary comae (Emery et al. 2006), we wanted to test similar particle sizes to those of comae. We tested a PSD of $0.1\text{--}0.5 \mu\text{m}$ with a peak at $0.2 \mu\text{m}$ based on cometary comae PSDs from Hanner et al. (1984), which resulted in a poorer fit or higher rms error between the modeled and measured spectra when compared to a single particle size. However, this does not mean that there is only one particle size on the surface of these asteroids but rather that our modeling emphasized the spectrally dominant particle size of the PSD present on the surface. The modeled PSD spectrum is plotted against a modeled spectrum of a single particle size in the Appendix, Figure 9(b).

In addition, we tested the effects of porosity on our model results. Despite the asteroid spectra resembling those of cometary comae (Hanner et al. 1994), we found that cometary comae-like porosities are not necessary to model the Trojan spectra, as previously proposed by Izawa et al. (2021) and Emery et al. (2006). We were able to model the Trojan and (944) Hidalgo spectra using porosities in the 70%–80% range, which is comparable to lunar regolith porosities of 74%–87% (Hapke & Sato 2016). These are lower porosities than cometary comae porosities, estimated to range from $\sim 84\%$ to 97% (Lasue et al. 2009). Figure 9 in Emery et al. (2006) shows the cometary spectra of Hale-Bopp and SW1 plotted against the spectrum of (624) Hektor. The cometary spectra have a significantly higher spectral contrast in their $10 \mu\text{m}$ plateau compared to the Trojans (Emery et al. 2006). This suggests that cometary spectra could possibly be modeled with lower porosities, since our modeling shows that spectral contrast increases with decreasing porosity (compare panels (a) and (c) in Figure 7). This range of porosities of the lunar regolith results from bombardment of the lunar surface over billions of years; on an airless body, impacts break up the surface rocks and regolith and scatter the fragments, leading to the present-day particle sizes and porosity (Fraknoi et al. 2016). Additionally, electrostatic dust lofting may be a contributor to the current porosity of the lunar regolith (Hood et al. 2018). Thus, we emphasize that cometary comae-like

porosities are not required to model the Trojan and (944) Hidalgo spectra, as previously thought.

Differences between the model fits and measured spectra were observed in all of the asteroid spectra (Figure 7). The peak in emissivity seen near $12 \mu\text{m}$ in all of the modeled spectra is a feature present in modeled crystalline fayalite and forsterite (see Figure 7) and San Carlos olivine laboratory spectra (Campins & Ryan 1989; Hamilton & Christensen 2000; Hamilton 2010). This peak is sharper in the modeled crystalline olivine compared to the laboratory spectra, which are more rounded (e.g., Figure 1 in Hamilton 2010). Also, there is a lack of a peak in laboratory amorphous olivine (e.g., Figure 1 in Dorschner et al. 1995). The dampening of the $12 \mu\text{m}$ peak in emissivity in the Trojan and (944) Hidalgo spectra is likely due to some low-albedo material mixing with the olivine to reduce this feature, along with amorphization of olivine. Space-weathering laboratory experiments have shown that crystalline olivine may be amorphized by solar wind (Yang et al. 2013). Since the Trojan spectra are missing this peak, we suggest that the Trojan surfaces have experienced some level of mixing in their surface regolith, meaning that we are measuring a spectral mixture of olivine with other low-albedo material(s) that exist on the asteroid surfaces and amorphization of olivine affecting the crystal structure of olivine present on their surfaces.

5. Conclusions

We modeled three Jupiter Trojan asteroids and (944) Hidalgo using a mixture of olivine components at 0.5 and $1.0 \mu\text{m}$ particle sizes with lunar-like porosities in order to fit their TIR spectra in the $\sim 7.5\text{--}13.5 \mu\text{m}$ region. Based on the results of this study, we anticipate that an intermediary olivine composition with approximately equal amounts of magnesium and iron would fit the (1172) Aneas and (944) Hidalgo spectra. However, these optical constants have yet to be measured and could not be used in this analysis. Asteroids (911) Agamemnon and (624) Hektor are both in the L4 group and were best fit using a 100% abundance of fayalite, suggesting a possible compositional difference between the L4 and L5 Trojan asteroids. However, with our small sample size, this is left as future work to include more Trojans in the L4 group. Our modeling results show that compositionally, the Trojan asteroids and (944) Hidalgo are consistent with the composition of spectrally similar bodies such as comet Hale-Bopp (very high porosity) and CO3 and CY chondrite meteorites (relatively low porosity). However, our modeled porosities that fit the asteroid spectra are not comparable to comet Hale-Bopp but are instead similar to those present on the lunar surface. Additionally, we showed that including a transparent matrix, such as a salt (e.g., halite), did not improve the model fit to the asteroid spectra.

Special thanks to Neil Bowles, Timothy Glotch, Audrey Martin, and Helena Bates for their assistance in this work. V.C. L., K.L.D.H., and H.C. are supported under NASA cooperative agreement 80NSSC19M0214 to the Center for Lunar and Asteroid Surface Science (CLASS) funded by NASA's Solar System Exploration Research Virtual Institute at the University of Central Florida. H.C. also acknowledges support from NASA's Near-Earth Object Observations program. G.I. is supported by a CNRS Momentum grant.

Appendix

Additional MSTM user-specified parameters include fixed versus random orientation of light, single particle size versus PSD, and rectangular versus spherical target. Fixed orientation of light accounts for the light source hitting the target (the collection of particles) from a single direction with the light rays in parallel. On the other hand, random orientation of light considers light incoming to the target from all directions and is more computationally expensive. The fixed orientation of light (Figure 9(a)), due to computational expense (>24 hr per one iteration or wavelength channel; 100 wavelength channels were computed), was used for the larger particle sizes of 1.0 and

$5.0 \mu\text{m}$. For particles of sizes less than $1.0 \mu\text{m}$, random orientation of light was chosen because the iterations are shorter for smaller particle sizes.

In Figure 9(a), there is a slight discrepancy between the fixed and random orientations for fayalite in the $0.5 \mu\text{m}$ particle size. We observed a large discrepancy between a single particle size versus a PSD in Figure 9(b). The single particle size resulted in a smaller rms error and overall better fit to the $10 \mu\text{m}$ plateau between measured and modeled asteroid spectra. There is little difference between the rectangular and spherical targets shown in Figure 9(c), especially in the region we modeled near $\sim 7.5\text{--}13.5 \mu\text{m}$, so the rectangular target was used in this work because this is the standard in previous uses of MSTM (Ito et al. 2017, 2018).

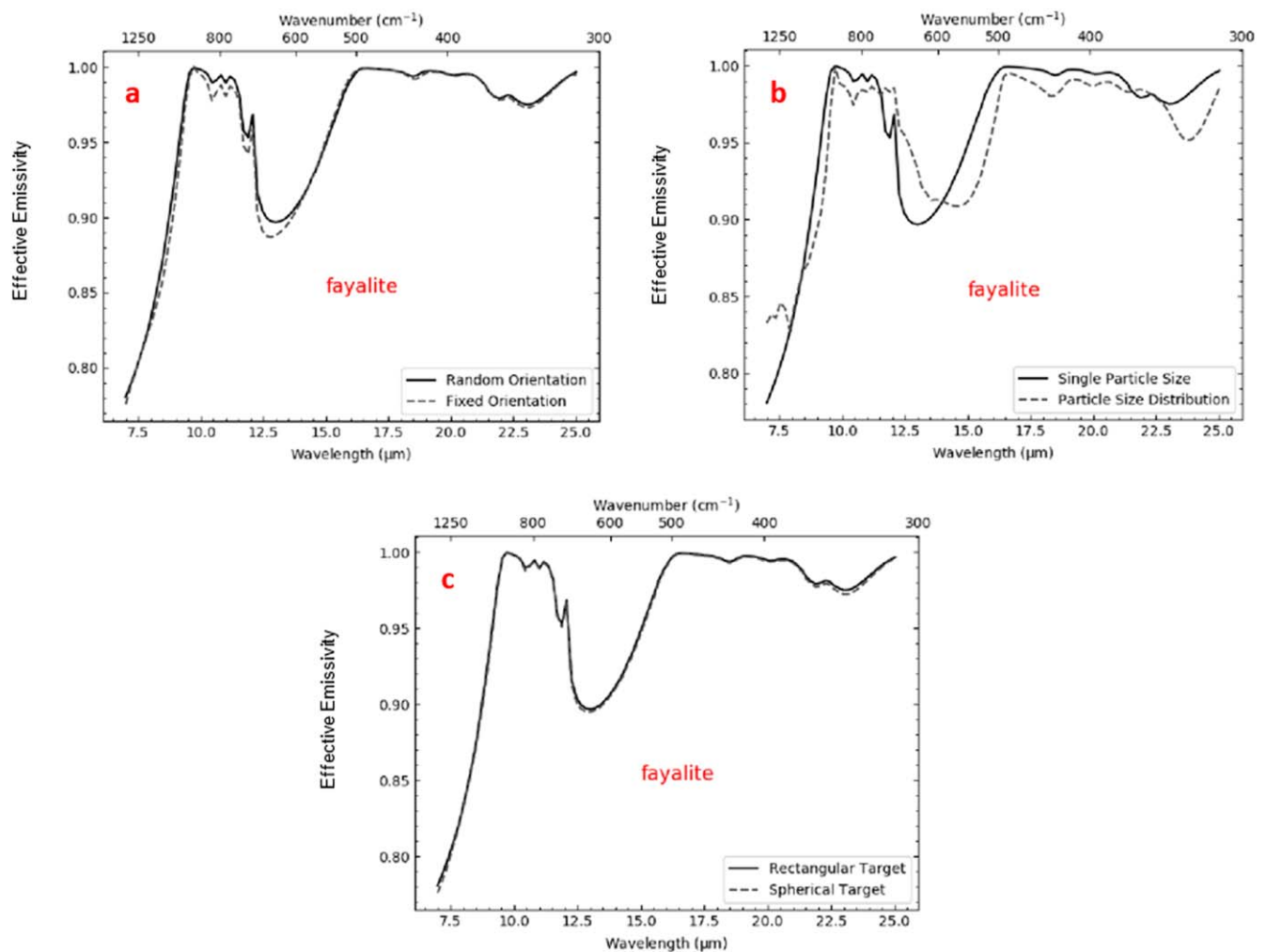






Figure 9. Comparison between random vs. fixed orientation of light (a), a single particle size vs. a PSD ($0.1\text{--}0.5 \mu\text{m}$ with a peak at $0.2 \mu\text{m}$) (b), and a rectangular vs. spherical target (c) for modeled fayalite. Panels (a), (b), and (c) show modeled fayalite at the $0.5 \mu\text{m}$ particle size.

ORCID iDs

Vanessa C. Lowry  <https://orcid.org/0000-0002-2721-9163>
 Gen Ito  <https://orcid.org/0000-0002-7350-6665>
 Michael S. P. Kelley  <https://orcid.org/0000-0002-6702-7676>
 Sean Lindsay  <https://orcid.org/0000-0002-6201-8789>

References

- Crisp, J., & Bartholomew, M. J. 1989, *LPSC*, **20**, 201
- Bates, H. C., Donaldson Hanna, K. L., King, A. J., et al. 2021, *JGRE*, **126**, e06827
- Brearley, A. J., & Jones, R. H. 1998, *Rev. Mineral. Geochem.*, **36**, 1, <https://pubs.geoscienceworld.org/msa/rimg/article/36/1/3-01/87383/chondritic-meteorites>
- Campins, H., Kelley, M. S., & Fernandez, Y. R. 2007, *AAS/DPS Meeting*, **39**, 486
- Campins, H., Licandro, J., Ziffer, J., et al. 2005, *AAS/DPS Meeting*, **37**, 645
- Campins, H., & Ryan, E. V. 1989, *ApJ*, **341**, 1059
- Carrier, W. D., III, Olhoef, G. R., & Mendell, W. 1991, *Lunar Sourcebook, A User's Guide to the Moon* (Cambridge: Cambridge Univ. Press), 475
- Christensen, P. R., Bandfield, J. L., Hamilton, V. E., et al. 2000, *JGR*, **105**, 9735
- Christensen, P. R., Bandfield, J. L., Hamilton, V. E., et al. 2001, *JGR*, **106**, 23823
- Christensen, P. R., Wyatt, M. B., Glotch, T. D., et al. 2005, *AGUFM*, **P13B–06**
- Conel, J. E. 1969, *JGR*, **74**, 1614
- Crovisier, J., Leech, K., Bokcelee-Morvan, D., et al. 1997, *Sci*, **275**, 1904
- Crovisier, J., Brooke, T. Y., Leech, K., et al. 2000, in *ASP Conf. Ser.* 196, *Thermal Emission Spectroscopy and Analysis of Dust, Disks, and Regoliths*, ed. M. L. Sitko et al. (San Francisco, CA: ASP), 109
- Donaldson Hanna, K. L., & Bowles, N. E. 2020, *LPSC*, **51**, 1062
- Dorschner, J., Begemann, B., Henning, Th., et al. 1995, *A&A*, **300**, 503
- Emery, J. P., & Brown, R. H. 2004, *Icar*, **170**, 131
- Emery, J. P., Burr, D. M., & Cruikshank, D. P. 2011, *AJ*, **141**, 25
- Emery, J. P., Cruikshank, D. P., & Van Cleve, J. 2006, *Icar*, **182**, 496
- Fraknoi, A., Morrison, D., & Wolff, S. C. 2016, *Astronomy* (1st ed.; Rice Univ.: OpenStax), 103
- Glotch, T. D. 2016, *JGRE*, **121**, 454
- Glotch, T. D., Christensen, P. R., & Sharp, T. G. 2006, *Icar*, **181**, 408
- Hamilton, V. E. 2000, *JGR*, **105**, 9701
- Hamilton, V. E. 2010, *ChEG*, **70**, 7
- Hamilton, V. E., & Christensen, P. R. 2000, *JGR*, **105**, 9717
- Hanner, M., Aitken, D., Roche, P., et al. 1984, *AJ*, **89**, 170
- Hanner, M., Lynch, D., & Russell, R. 1994, *ApJ*, **425**, 274
- Hapke, B. 1993, *Theory of Reflectance and Emittance Spectroscopy* (1st ed.; Cambridge: Cambridge Univ. Press)
- Hapke, B. 2012, *Theory of Reflectance and Emittance Spectroscopy* (2nd ed.; Cambridge: Cambridge Univ. Press)
- Hapke, B., & Sato, H. 2016, *Icar*, **273**, 75
- Hargrove, K., Campins, H., Kelley, M., et al. 2008, *AGUSM*, **P34A–06**
- Harker, D. E., Wooden, D. H., Woodward, C. E., et al. 2002, *ApJ*, **580**, 579
- Harker, D. E., Wooden, D. H., Woodward, C. E., et al. 2004, *ApJ*, **615**, 1081
- Harris, A. 1998, *Icar*, **131**, 291
- Henderson, B. G., & Jakosky, B. M. 1994, *JGR*, **99**, 19,063
- Henning, T., & Stognienko, R. 1996, *A&A*, **311**, 291
- Hood, N., Carroll, A., Mike, R., et al. 2018, *GeoRL*, **45**, 13,206
- Hörz, F., & Cintala, M. 1997, *M&PS*, **32**, 179
- Houck, J. R., Roelling, T. L., van Cleve, J., et al. 2004, *ApJS*, **154**, 18
- Ito, G., Arnold, J. A., & Glotch, T. D. 2017, *JGRE*, **122**, 822
- Ito, G., Mischenko, M. I., & Glotch, T. D. 2018, *JGRE*, **123**, 1203
- Izawa, M., King, P., Vernazza, P., Berger, J. A., McCutcheon, W. A., et al. 2021, *Icar*, **359**, 114328
- Koepfen, W. C., & Hamilton, V. E. 2008, *JGR*, **113**, E05001
- Lasue, J., Levasseur-Regourd, A. C., Hadamcik, E., et al. 2009, *Icar*, **199**, 129
- Licandro, J., Hargrove, K., Kelley, M., et al. 2012, *A&A*, **537**, A73
- Lisse, C. M., Kraemer, K. E., Nuth, J. A., III, et al. 2007, *Icar*, **187**, 69
- Lowry, V. C., Donaldson Hanna, K. L., Campins, H., et al. 2022, *E&SS*, **9**, e02146
- Lyon, R. J. P. 1964, *Evaluation of Infrared Spectrophotometry for Compositional Analysis of Lunar and Planetary Soils* NASr-49(04), Stanford Research Inst., <https://ntrs.nasa.gov/api/citations/19650001173/downloads/19650001173.pdf>
- Mackowski, D. 2013, *MSTM version 3.0*, <https://www.eng.auburn.edu/~dmckwski/scatcodes>
- Mackowski, D., & Mischenko, M. 1996, *JOSAA*, **13**, 2266
- Mackowski, D., & Mischenko, M. 2011, *JQSRT*, **112**, 2182
- Martin, A. C., Emery, J. P., & Loeffler, M. J. 2022, *Icar*, **378**, 114921
- Marzari, F., School, H., Murray, C., et al. 2002, in *Asteroids III*, ed. W. F. Bottke, Jr. (Tucson, AZ: Univ. Arizona Press), 725
- Moersch, J. E., & Christensen, P. R. 1995, *JGR*, **100**, 7465
- Mottola, S., Di Martino, M., Erikson, A., et al. 2011, *AJ*, **141**, 170
- Mueller, M. 2018, *Asteroid Thermal Emission Following the Near-earth Asteroid Thermal Model* <https://github.com/MigoMueller/NEATM>
- Mustard, J. F., & Hays, J. E. 1997, *Icar*, **125**, 145
- Ramsey, M. S., & Christensen, P. R. 1998, *JGR*, **103**, 577
- Rivkin, A., Emery, J., Barucci, A., et al. 2009, *The Trojan Asteroids: Keys to Many Locks*, Johns Hopkins University/Applied Physics Laboratory <https://ia800504.us.archive.org/24/items/TheTrojanAsteroids-KeystoManyLocks/AndrewSRivkin-trojans.pdf>
- Rogers, A. D., & Aharonson, O. 2008, *JGRE*, **113**, E06S14
- Roush, T., Pollack, J., & Orenberg, J. 1991, *Icar*, **94**, 191
- Salisbury, J., & Eastes, J. W. 1985, *Icar*, **64**, 586
- Salisbury, J., & Wald, A. 1992, *Icar*, **96**, 121
- Salisbury, J., & Walter, L. 1989, *JGR*, **94**, 9192
- Scott, A., & Duley, W. W. 1996, *ApJS*, **105**, 401
- Singleton, E. B., & Shirkey, C. T. 1983, *ApOpt*, **22**, 185
- Spitzer Science Center 2012, *IRS Instrument Handbook* Pasadena Spitzer Science Center, <https://irsa.ipac.caltech.edu/data/SPITZER/docs/irs/irsinstrumenthandbook/4/>
- Sprague, A. L., Emery, J. P., Donaldson Hanna, K. L., et al. 2002, *M&PS*, **37**, 1255
- Sprague, A. L., Witteborn, F. C., Kozłowski, R. W., et al. 1992, *Icar*, **100**, 73
- Stokes 1992, *UCF Advanced Research Computing Center Stokes General-purpose Cluster*, <https://arc.ist.ucf.edu/index.php/resources/stokes/about-stokes>
- Usui, F., Kuroda, D., Müller, T. G., et al. 2011, *PASJ*, **63**, 1117
- Vernazza, P., Delbo, M., King, P. L., et al. 2012, *Icar*, **221**, 1162
- Wald, A., & Salisbury, J. 1995, *JGR*, **100**, 24665
- Watanabe, H., & Matsuo, K. 2003, *GesJ*, **7**, 347
- Yang, B., Lucey, P., & Glotch, T. 2013, *Icar*, **223**, 359
- Yang Li, X. L., Wang, S., Li, S., et al. 2013, *JGRE*, **118**, 1974